

Article

Flow Characteristics and Parameter Influence of the Under-Expansion Jet on Circulation Control Airfoil

Meng He, Liu Zhang *, Chang Li and Lei Zhao

Low Speed Aerodynamics Institute, China Aerodynamics Research & Development Center, Mianyang 621000, China; hemeng@cardc.cn (M.H.)

* Correspondence: lzh2607@cardc.cn

Abstract: The enhancement in the jet pressure ratio and jet velocity contributes to expanding the control efficiency and control boundary of circulation control airfoil under high subsonic incoming flow. However, because of an excessive jet pressure ratio, the jet separates prematurely on the Coanda surface, resulting in control failure. In a bid to improve the adhesion capability of the jet under a high pressure ratio, a circulation control airfoil with a converging nozzle and back-facing step structure at the trailing edge was numerically simulated based on the Reynolds averaged Navier–Stokes equation (RANS), and a study was conducted on the complex flow structure of the under-expansion jet on the Coanda surface and the impact of design parameters such as jet pressure ratio, ellipticity, and nozzle height on the jet separation. The results show that the back-facing step provides an expansion space for the under-expansion jet and changes the shock-boundary layer interaction form. As the jet pressure ratio and nozzle height increase, the size of the shock cell increases, the strength of the intercepting shocks on both sides increases, and Mach reflection occurs, resulting in jet stratification and in a decline in the adhesion capability of the jet. The combination design of proper ellipticity and the back-facing step contributes to forming a closed low-pressure vortex area behind the step and promote jet attachment. Reducing the nozzle height can improve the adhesion capability of the jet under a high pressure ratio.

Keywords: circulation control; under-expansion jet; shock structure; flow control



Citation: He, M.; Zhang, L.; Li, C.; Zhao, L. Flow Characteristics and Parameter Influence of the Under-Expansion Jet on Circulation Control Airfoil. *Energies* **2023**, *16*, 3818. <https://doi.org/10.3390/en16093818>

Academic Editor: Bjørn H. Hjertager

Received: 7 March 2023

Revised: 3 April 2023

Accepted: 20 April 2023

Published: 29 April 2023



Copyright: © 2023 by the authors. Licensee MDPI, Basel, Switzerland. This article is an open access article distributed under the terms and conditions of the Creative Commons Attribution (CC BY) license (<https://creativecommons.org/licenses/by/4.0/>).

1. Introduction

In the 1930s, Henry Coanda [1], a Romanian engineer, found that when a fluid moves along a convex wall, it tends to flow on the surface of an object due to the balance between the pressure difference in the fluid and the centripetal force moving around the curved surface. Many flow control studies have been carried out based on this physical phenomenon, and circulation control (CC) is a typical application. CC airfoil is when the trailing edge of the airfoil is partially truncated and changed into a circular arc, and a plenum chamber is arranged inside the airfoil. The compressed gas is tangentially ejected from the slot along the arc of the trailing edge, and the jet is able to move on the circular arc wall under the action of the Coanda effect. The flow on the upper airfoil is accelerated by the entrainment of a high-speed jet, the stagnation point on the leading edge moves down along the pressure surface, and the separation point on the trailing edge moves to the lower surface, thus resulting in an increase in the circulation and lift in the airfoil.

There have been many wind tunnel tests based on CC airfoil. Using the wind tunnel test [2,3], Englar analyzed the lift augmentation effect of 15% thick elliptical airfoil at subsonic and transonic speeds under design parameters such as different nozzle heights and Coanda profiles, and determined the optimal design range of CC parameters. Englar further applied CC to supercritical airfoil [4], so that the airfoil had an excellent cruise performance and high lift characteristics through reasonable parameter design. Through the wind tunnel test [5], Abramson analyzed the lift augmentation capability of two CC

airfoils with 15% thickness and 1% camber at subsonic speed under different angles of attack and blowing momentum coefficients. Novak studied the aerodynamic characteristics of CC airfoil at 0.12 Ma through the wind tunnel test [6]. In this experiment, different stations were measured using a laser velocimeter to obtain the data of the velocity profile and turbulent Reynolds stress on the Coanda surface for CFD verification. The thickness of the CC airfoil studied in previous wind tunnel tests basically exceeded 15%. Alexander [7] analyzed the influence law and aerodynamic performance of the nozzle height and the Coanda profile parameters of elliptical CC airfoil with 6% thickness and 0.75% camber in a NASA Langley Transonic Dynamics Tunnel (TDT), which filled the research gap of thin airfoils at a high Mach number.

With the development of CFD technology, numerical calculation is an important development direction to predict the aerodynamic characteristics of CC airfoil. Swanson [8] and Rumsey calculated Novak's test model [6] based on the CFL3D program. The results reveal that a turbulence model with curvature correction can better solve the problem of high-speed fluid flowing around the Coanda surface, but the calculated lift coefficient is larger than the test result. Nishino [9] analyzed the turbulence structure and physical characteristics near the exit of the Coanda jet in detail using large eddy simulation (LES). Rumsey compared the difference between RANS and LES methods based on the GTRI model [10], and studied the impact of grid density, compressible and incompressible solvers, and turbulence models on the calculation results. The results show that three turbulence models (including SSTRC, SARC, and EASM-ko) can capture the position of jet separation reasonably well, and SARC is the best for predicting the flow very near the Coanda surface.

Among the current CFD numerical methods, because of the limitation of computing resources and time cost, the RANS equation is still the main tool for engineering application research. Previous research results show that the SARC turbulence model can more accurately simulate the jet flow structure of CC airfoil and capture the position of jet separation. Therefore, this paper adopts the RANS equation and SARC turbulence model for numerical simulation.

Initially, CC was mainly used to increase lift and improve the short takeoff and landing (STOL) performance of aircraft. However, as the Mach number of free incoming flow increased, the lift augmentation efficiency of CC dropped sharply, and a huge amount of bleed also limited its application potential. Later, researchers found that CC can also substitute the mechanical rudder surface to realize aircraft attitude control, and the bleed required is small, which has become a hot research topic at present. For example, Lockheed proposed the "Innovative Control Effectors (ICE)" plan [11], NATO AVT-239 task group [12], and successfully performed flight verification at low speeds, for example using DEMON UAV [13] and MAGMA UAV Demonstrator [14]. Through a powered virtual flight test in a wind tunnel [15], the China Aerodynamics Research and Development Center verified the rudderless flight control of a tailless flying wing in pitch and roll attitudes based on CC, and responded rapidly. The studies above preliminarily show the application prospect of CC for improving the stealth and maneuver control characteristics of flying wing aircraft.

In order to meet the rudderless jet flight attitude control requirements of aircraft in a wide velocity domain and to expand the application range of CC technology, the supersonic jet needs to improve its control efficiency at a high subsonic velocity incoming flow. However, the supersonic jet is easy to separate prematurely on the Coanda surface, resulting in control failure. It has been found that this problem can be solved by using a converging nozzle and back-facing step structure [16,17] or elliptical Coanda profile [2], but there are few studies on their combination design in the existing literature. During combination design, there is a lack of systematic research on the impact of different parameters on the aerodynamic characteristics and trailing edge flow field structure of CC airfoil. Moreover, CC airfoil adopts blunt trailing edge and is not constrained by the Kuta condition. Consequently, its aerodynamic characteristics and flow field structure are very sensitive to the geometric parameters of the jet device, and a systematic analysis of the effect of the design parameters on CC characteristics will help guide the design of CC airfoil.

In this paper, we extensively studied the impact of the back-facing step on the attachment flow characteristics of the under-expansion jet from the converging nozzle on the curved wall; analyzed the impact of design parameters such as jet pressure ratio, ellipticity, and nozzle height on the aerodynamic characteristics and flow field structure of CC airfoil; and mastered the separation control methods that affect the attachment of the under-expansion jet, which provides a reference for CC design at high subsonic speeds.

This paper is arranged as follows: firstly, the proposed reference airfoil is introduced and the design parameters are described. Section 2 describes the numerical methods. The accuracy of the solver is verified. Section 3 analyzes the numerical calculation results and the final section lists out the conclusions.

2. CC Airfoil

The computational model is inspired by the wing root profile airfoil of a subsonic UAV. The airfoil chord is normalized ($c = 1.0$ m) and the maximum thickness is $11.5\%c$. The initial airfoil and the trailing edge comparison between the initial airfoil and CC airfoil are shown in Figure 1. The definitions of geometric parameters such as the back-facing step size (t), Coanda profile, and nozzle height (h) are shown in Figure 2, and the variation range of design parameters is shown in Table 1. The thickness of the trailing edge above the jet nozzle is 1 mm, and the Coanda profile is elliptical. The semi-minor axis b is 4.5 mm, the ratio of the length of the major axis a to the minor axis b is defined as the ellipticity (a/b), and the height of the back-facing step (t) is 0.5 mm.

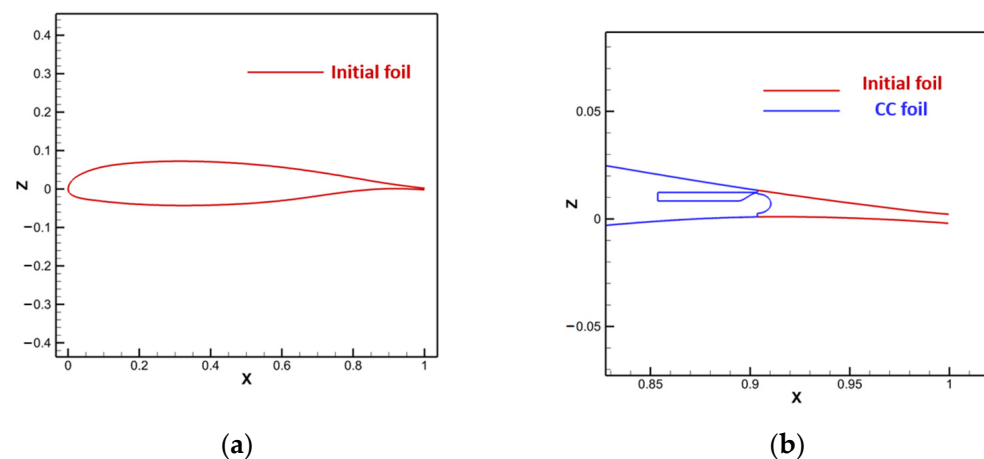


Figure 1. CC airfoil and trailing edge structure: (a) initial airfoil; (b) comparison of trailing edges between the initial airfoil and CC airfoil.

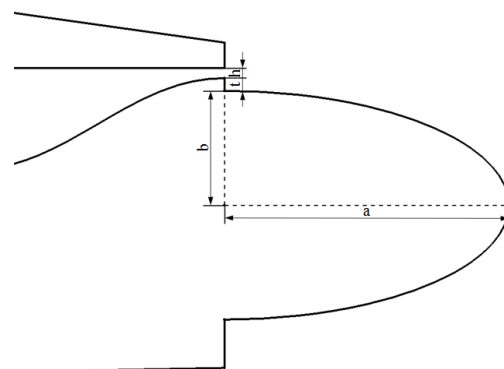


Figure 2. Geometric parameters.

Table 1. Design parameters.

Design Parameters	Value Range
Jet pressure ratio, (<i>NPR</i>)	2, 3, 4, 5, 6, 7, 8
Ellipticity, (<i>a/b</i>)	1.0, 1.5, 2.0
Nozzle height, (<i>h</i>), mm	0.1, 0.2, 0.3

3. Numerical Solution Method

The flow field of CC airfoil is predicted by the RANS equation. The turbulence model is a SA model and adopts compressibility correction and curvature correction. Space discretization is based on the lattice-centered finite volume method of a mixed unstructured grid, the flux adopts Reo format, and the LU_SGS method is adopted for time advancing.

3.1. Verification of Calculation Accuracy of CC Airfoil

The accuracy of the solver is verified by the CC airfoil test conducted by Alexander et al. [7] in NASA Langley TDT. The test model is an elliptical airfoil with a chord length of 30 inches and a span of 60 inches, without sweepback. An end plate is arranged at the wing end to eliminate the effect of 3D flow. The maximum thickness of the airfoil is $6\%c$ and the camber is $0.75\%c$. The airfoil is truncated at 90% of the trailing edge, and a Coanda profile is arranged as shown in Figure 3. The diameter of the test end plate is 1 times the airfoil chord. To facilitate grid generation, the diameter of the end plate is 1.1 times the chord in calculation, so that the grid topology is easily divided at the leading edge of the airfoil [18].

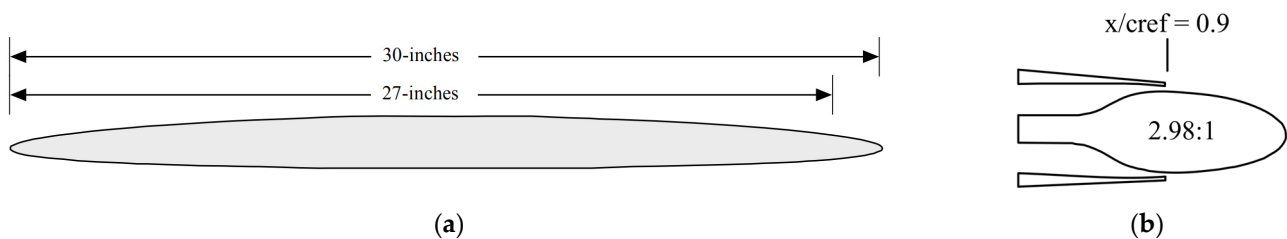


Figure 3. CC airfoil [7]: (a) basic elliptical airfoil section; (b) Coanda surface.

The test model is shown in Figure 4. The numerical calculation shows that the far field is 10 times the chord in the radial direction and 7 times the chord in the spanwise direction. The distance of the first grid point near the wall is held constant to maintain $y^+ \sim O(1)$. Three sets of grids (3300 w, 1600 w, and 800 w, respectively) are generated to verify the convergence. The surface grid is shown in Figure 5.

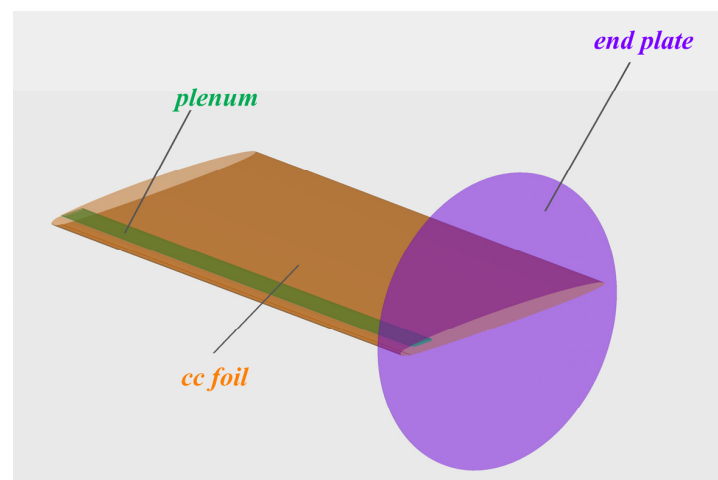


Figure 4. Schematic diagram of the test model.

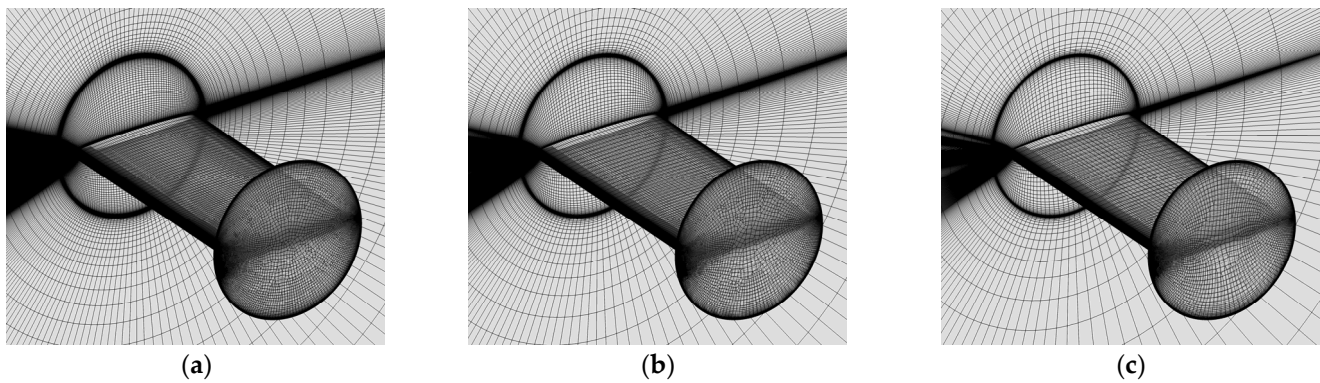


Figure 5. Surface grid: (a) fine grid; (b) medium grid; (c) coarse grid.

The jet momentum is measured by the blowing momentum coefficient C_μ , which is defined as follows:

$$C_\mu = \frac{\dot{m}V_{\text{jet}}}{q_\infty S} \quad (1)$$

wherein \dot{m} is the mass flow at the jet exit, V_{jet} is the jet velocity at the exit, q_∞ is the dynamic pressure of the freestream flow, and S is the reference area.

The exit jet velocity V_{jet} can be calculated using Equation (2):

$$V_{\text{jet}} = \sqrt{2RT_0 \frac{\gamma}{\gamma-1} \left[1 - \left(\frac{P_\infty}{P_0} \right)^{\frac{\gamma-1}{\gamma}} \right]} \quad (2)$$

wherein P_0 is the total pressure of jet plenum, T_0 is the total temperature of the plenum, and γ is the specific heat ratios. The blowing momentum coefficient depends on the given total temperature and total pressure at the inlet of the jet plenum.

The freestream flow conditions are set to $Ma = 0.7$, $Re = 2.5 \times 10^6$, and $\alpha = 3^\circ$. The states when there is no jet and the blowing momentum coefficient $C_\mu = 0.006$ are calculated separately.

Figure 6a shows the calculation results under different grid sizes without jet flow. The results show that the pressure distribution calculated by different grid sizes basically coincides with the test pressure coefficient. The difference in grid influence can be ignored, and the peak negative pressure at the leading edge is higher than the test value. As the plane at the connection between the model and the wind tunnel is set to the symmetric plane under the given boundary conditions, the calculation results may be slightly different from the test values. Figure 6b compares the numerical calculation results of the fine grid with the test values at $C_\mu = 0.006$, and shows that the pressure distribution on the upper and lower airfoils and the Coanda profile coincide with the test values, and the calculated peak negative pressure at the leading edge is slightly higher. To sum up, the numerical method adopted and the grid setting can reasonably predict the flow field of CC airfoil and basically meet the required calculation accuracy.

3.2. Verification of Calculation Accuracy of Supersonic Coanda Jet

In order to further evaluate the simulation accuracy of the solver on the flow field characteristics of supersonic jet flow on the Coanda profile, the static jet deflection test [19] conducted by Llopis at a higher jet pressure ratio is performed for verification. The test device is shown in Figure 7. The test uses a converging–diverging nozzle, and the Coanda profile is a 90° arc, with a radius of $R = 100$ mm and a nozzle height of $h = 10$ mm, $h/R = 0.1$. In this paper, a converging–diverging nozzle with a design pressure ratio of 4 is used for the numerical simulation.

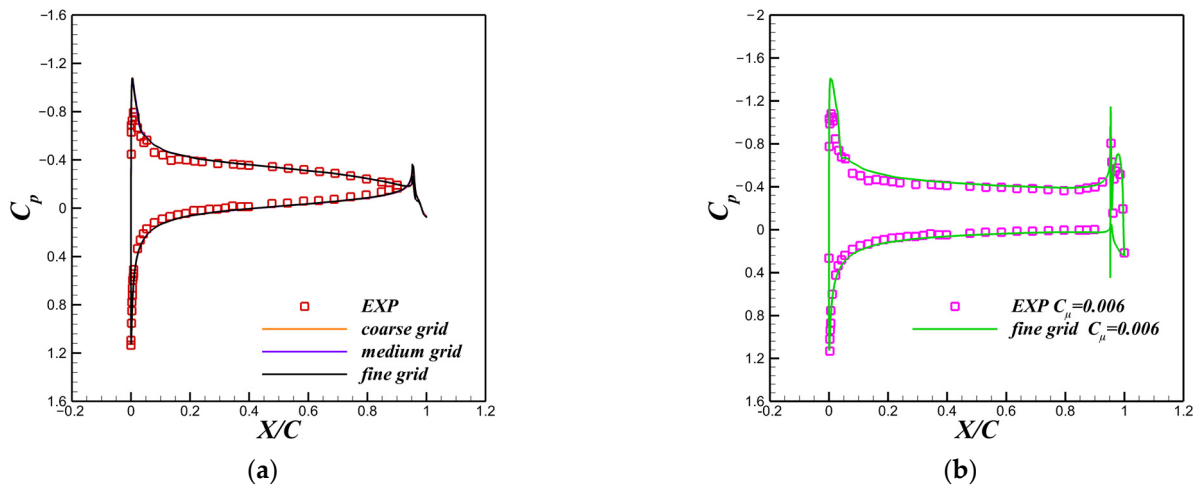


Figure 6. Comparison of pressure distribution on airfoil surface: (a) Without jet flow; (b) With jet flow.

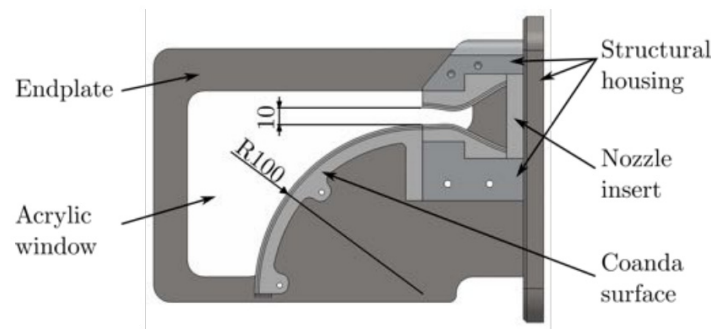


Figure 7. Side projection of the static jet deflection test device.

The computational domain and boundary conditions are shown in Figure 8a, and the computational grid is shown in Figure 8b. The upper, lower, and right far-field distances are 50 R. The setting of far-field distance and boundary conditions refer to the numerical simulation conducted by Qing Wang et al. [20]. A structured grid is adopted. The distance of the first grid point near the wall was held constant to maintain $y^+ \sim O(1)$, and the grid size is 140,000. At the ambient pressure $P_{atm} = 100,000$ Pa and the temperature $T = 300$ K, the flow field under different jet pressure ratios ($\frac{P_0}{P_{atm}}$) is calculated separately, and the pressure coefficient is defined as follows:

$$C_p = \frac{P - P_{atm}}{P_{plenum} - P_{atm}} \tag{3}$$

Figure 9 shows a comparison between the calculated value and the experimental value of the pressure coefficient on the Coanda surface under different jet pressure ratios. The results reveal that, under different jet pressure ratios, the calculation results can basically capture the variation in pressure distribution on the Coanda surface, which coincides with the variation trend of the test results. According to other literature [8–10], different turbulence models cannot accurately capture the flow field characteristic details of the Coanda surface, and the calculation results of different turbulence models differ. When the jet pressure ratio is 5.6, the jet is still attached to the Coanda surface, and the calculated value of the pressure coefficient on the Coanda surface agrees well with the experimental value. When the jet pressure ratio is 6.1, the jet is separated from the Coanda surface, and the calculation results also agree well with the experimental results, indicating that the numerical method proposed can accurately capture the separation pressure ratio, and meets the simulation requirements of the supersonic jet on the Coanda surface.

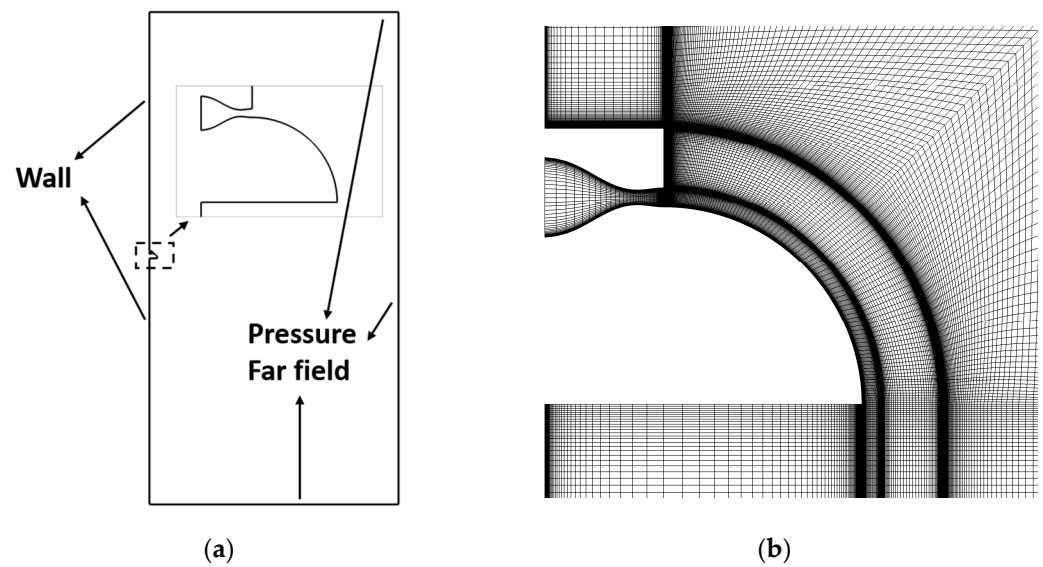


Figure 8. Computational domain and computational grid: (a) computational domain and boundary conditions and (b) computational grid.

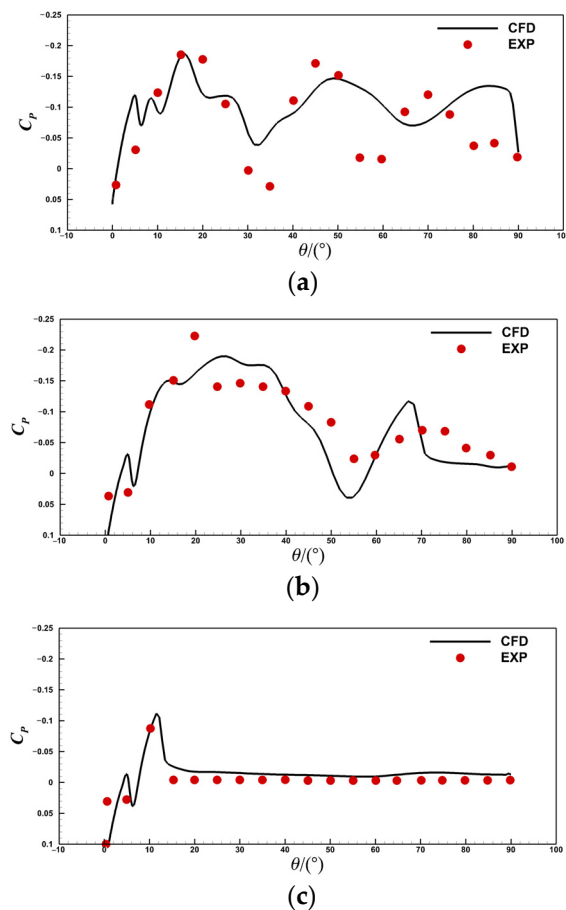


Figure 9. Comparison of pressure distribution on the Coanda surface: (a) $\frac{P_0}{P_{atm}} = 4.1$; (b) $\frac{P_0}{P_{atm}} = 5.6$; (c) $\frac{P_0}{P_{atm}} = 6.1$.

4. Analysis of Flow Characteristics of the Under-Expansion Jet

The freestream flow conditions are set to $Ma = 0.6$, $Re = 6.362 \times 10^6$ and $\alpha = 3^\circ$. The far field is set to the velocity inlet boundary condition. It is considered that there is a stable air source in the jet chamber. The inlet is set as the boundary condition with the total

pressure P_0 and total temperature T_0 . The total pressure P_0 is determined by the product of the static pressure P_∞ of the free incoming flow and the jet pressure ratio (NPR), that is, $P_0 = P_\infty \times NPR$, $T_0 = 288$ K. The airfoil surface, Coanda surface, and jet channel surface are treated as a no-slip wall.

The computational grid is a structured grid with a computational domain of $40c \times 40c$. The distance of the first grid point near the wall was held constant to maintain $y^+ \sim O(1)$. The grid is shown in Figure 10. Three sets of grids, namely, L0 (440,000), L1 (260,000), and L2 (110,000), are generated, respectively. The aerodynamic force results are shown in Table 2. At the same angle of attack and jet pressure ratio, the lift coefficient of the L2 grid is increased by 0.0312 and that of the L0 grid is decreased by 0.0018 compared with the L1 grid, indicating that the calculation accuracy of the 440,000 grid is comparable to that of the 260,000 grid. Figure 11 shows a comparison of the pressure coefficients on the airfoil surface under different grid sizes. The results show that the grid size has little impact on the distribution of the pressure coefficients, and the pressure distribution of the L0 grid agrees well with that of the L1 grid. Therefore, a 260,000 grid is used to evaluate the aerodynamic characteristics of CC airfoil.

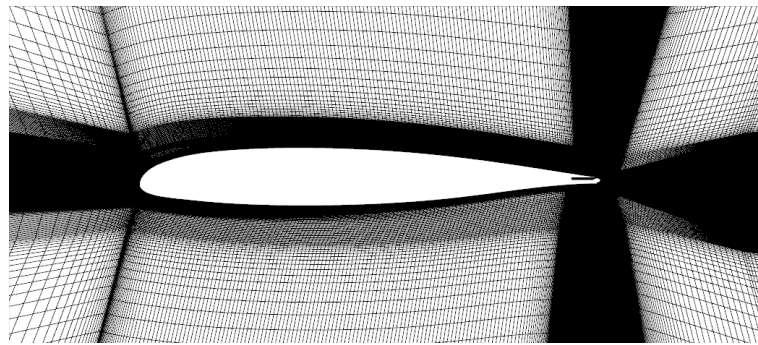


Figure 10. Structured grid of the CC airfoil.

Table 2. Grid convergence.

Grid Size	$\alpha/(\circ)$	C_L	C_D	NPR
L0	0	0.4276	0.010256	4
L1	0	0.4258	0.010248	4
L2	0	0.4570	0.010657	4

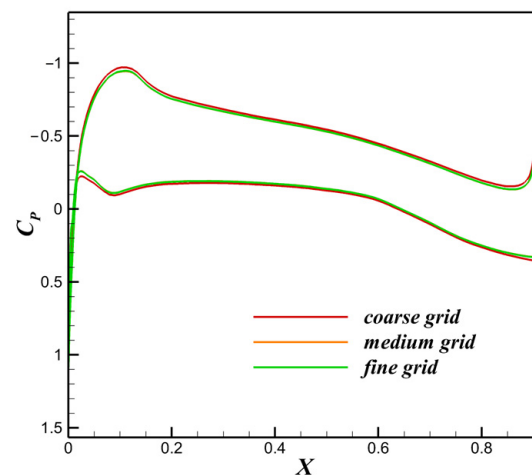


Figure 11. Surface pressure coefficient of $NPR = 4.0$.

4.1. Analysis of Flow Field Structure under Different Jet Pressure Ratios

A configuration with ellipticity $a/b = 1.5$, nozzle height $h = 0.2$ mm, and back-facing step height $t = 0.5$ mm is selected to study the impact of different jet pressure ratios on the aerodynamic characteristics and flow field structure of CC airfoil.

The variation trend in lift coefficient (C_L) with the jet pressure ratio is shown in Figure 12. As the jet pressure ratio increases, the lift coefficient increases and then decreases, and reaches the maximum value when the pressure ratio is $NPR = 6$. The jet pressure ratio when the lift coefficient starts to decrease with the increase in pressure ratio is called the critical stall pressure ratio.

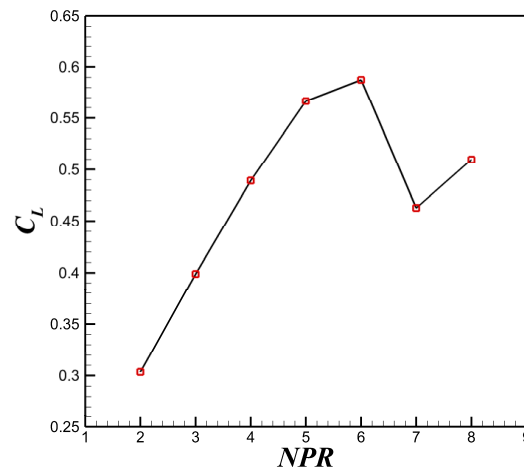


Figure 12. Variation trend in lift coefficient with the jet pressure ratio.

Figure 13 shows the pressure coefficients on the airfoil surface under different jet pressure ratios. With the increase in jet pressure ratio, the entrainment effect of the jet on the upper airfoil is enhanced, the velocity on the upper airfoil increases and the surface pressure coefficient decreases. The “virtual rudder surface” formed by the jet blocks the flow of the lower airfoil, the velocity on the lower airfoil decreases, and the pressure coefficient on the lower airfoil increases. As the jet pressure ratio increases, the stagnation point at the leading edge moves backward, the upwash effect is enhanced, and the peak negative pressure at the leading edge increases. However, when the jet pressure ratio exceeds the critical stall pressure ratio, the stagnation points at the trailing and leading edges move forward, and the acceleration effect of the jet on the upper airfoil and the blocking effect of the jet on the lower airfoil are weakened. Thus, the lift coefficient decreases.

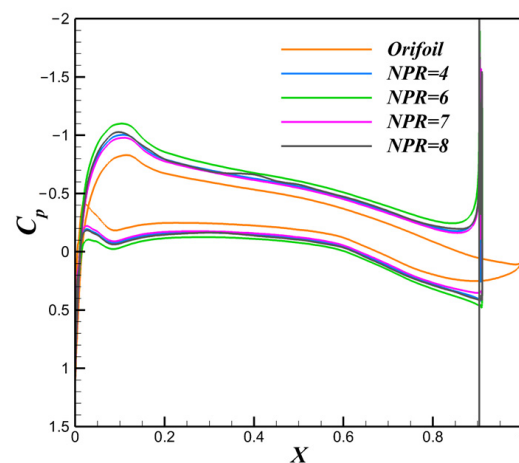


Figure 13. Airfoil surface pressure coefficient.

Figure 14 shows the Mach number cloud diagram at the jet exit, and Figure 15 shows the Schlieren image rendered by the density gradient of the flow field. The under-expansion jet reaches sound velocity at the exit throat, forming a quasi-periodic shock structure different from that of the subsonic jet at the exit. In addition, the size of the shock cell increases with the increase in the jet pressure ratio.

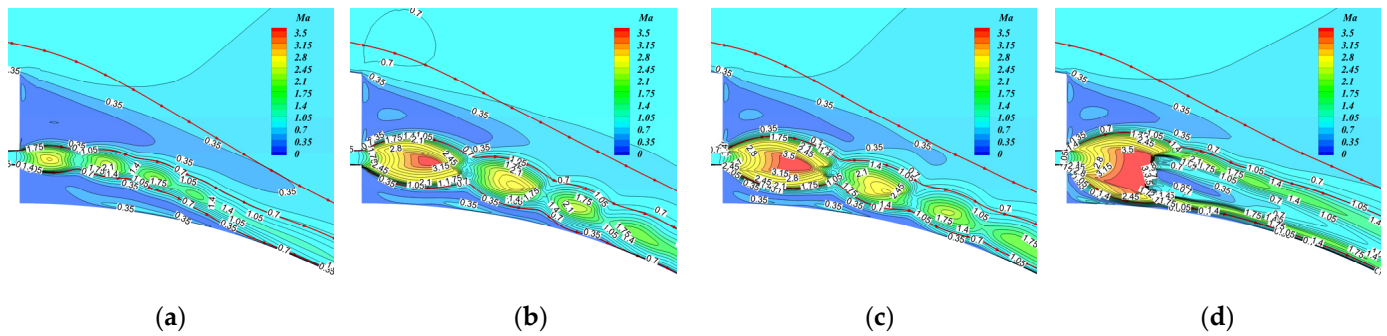


Figure 14. Mach number cloud diagram at the jet exit: (a) $NPR = 4$, (b) $NPR = 6$, (c) $NPR = 7$, and (d) $NPR = 8$.

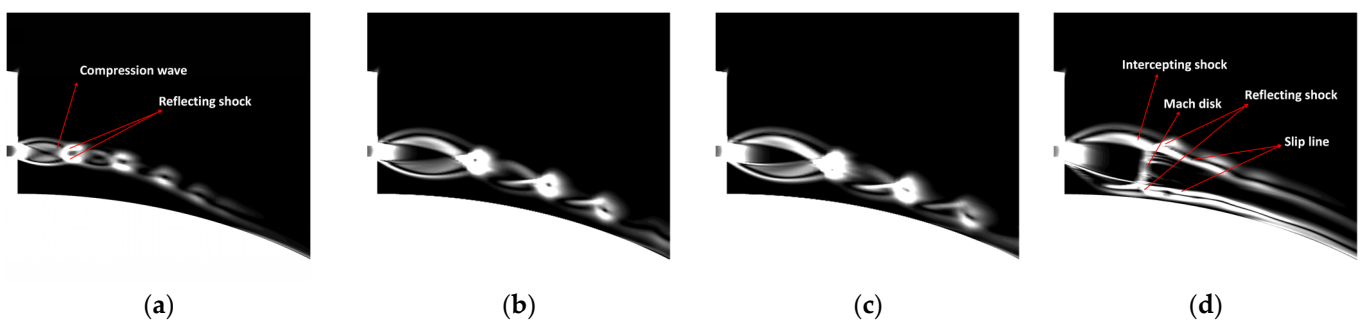


Figure 15. Schlieren image: (a) $NPR = 4$, (b) $NPR = 6$, (c) $NPR = 7$, and (d) $NPR = 8$.

The jet expands rapidly at the exit, forming an expansion wave. The existence of a step below the jet nozzle transforms the shock–boundary layer interaction into a shock–shear layer interaction. The trailing edge above the jet nozzle is 1 mm thick, and the jet interacts with the airfoil shear layer. The expansion waves on both sides of the jet are reflected by the shear layer, forming a compression wave. The compression waves then merge to form an intercepting shock. As the jet pressure ratio increases, the strength of intercepting shock increases, and the intercepting shocks on both sides meet to form a reflecting shock. The reflecting shock meets with the jet boundary and is reflected as an expansion wave. The entire process starts to repeat. Finally, under the action of viscosity, the jet energy decays and shock cells disappear. At $NPR = 8$, the intercepting shocks on both sides meet and generate Mach reflection. A strong Mach disk structure and reflecting shocks are formed in the shock cell, but no periodic shock structure is formed. After the normal shock (Mach disk), the jet is subsonic, and a reflecting shock becomes an oblique shock. The jet remains supersonic after passing through the oblique shock. A slip line is formed between the flows on both sides. On both sides of the slip line, the static pressure and flow direction of the jet are the same, but the velocity is different.

Figure 16b,c shows the pressure coefficient and tangential velocity, respectively, on the Coanda surface under different jet pressure ratios. The definitions of θ and V_t are shown in Figure 16a. The flow behind the step is partially taken away by the entrainment of the high-speed jet. In the absence of air supply, a low-pressure vortex is formed in the area behind the step. The jet is attached to the wall under the centripetal force provided by the pressure difference on both sides. When the jet pressure ratio NPR increases from 4 to 6, the entrainment effect of the jet on the low-pressure area is enhanced and the pressure

difference increases. However, when the jet pressure ratio increases again, the adhesion capability of the jet on the Coanda surface is reduced, and the entrainment effect on the low-pressure area declines. At $NPR = 8$, the size of the shock cell increases significantly, which reduces the range of low-pressure area behind the step, and limits the effect of the low-pressure area.

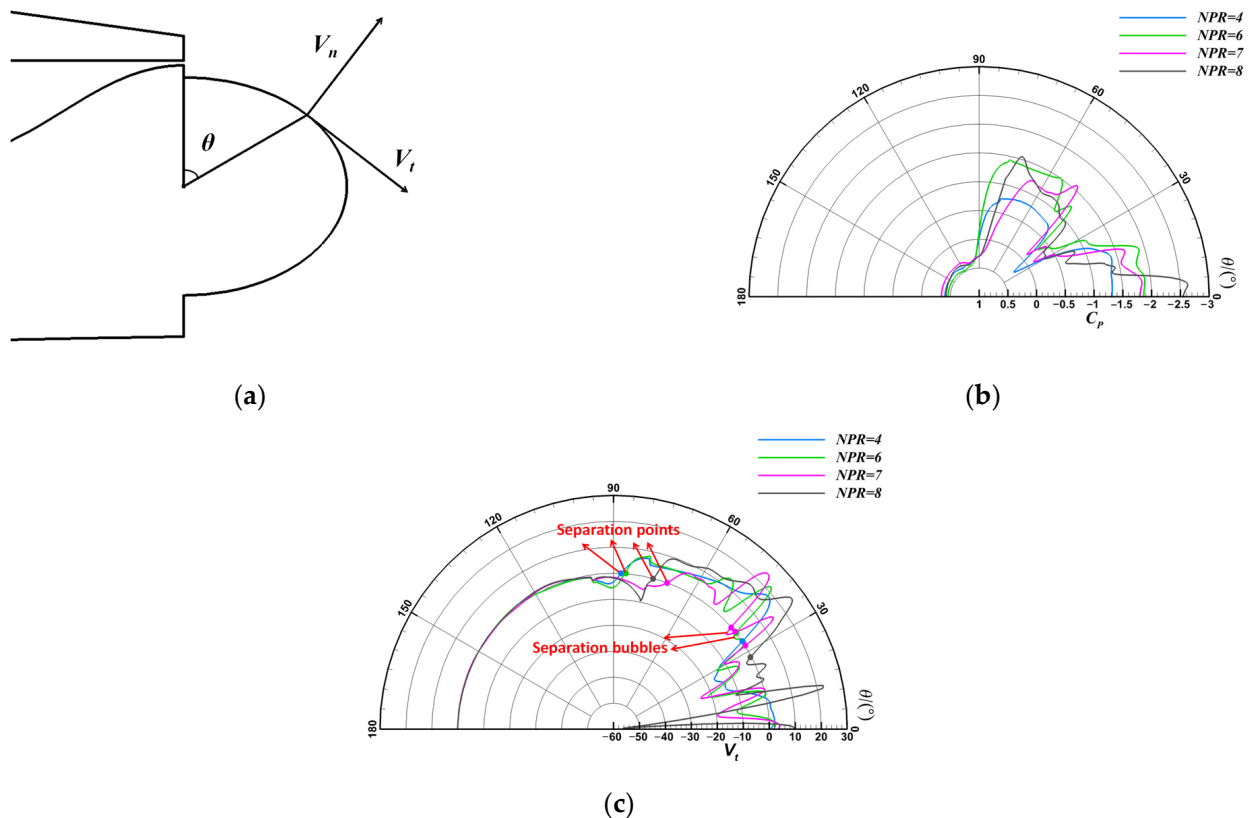


Figure 16. Comparison of the pressure coefficient and tangential velocity on the Coanda surface: (a) parameter definition, (b) comparison of pressure coefficient on the Coanda surface, and (c) comparison of tangential velocity on the Coanda surface.

At about $\theta = 30^\circ$, under the action of compression waves in a shock cell, there is an unfavorable reverse pressure gradient on the Coanda surface, which easily causes separation. Under the action of expansion waves in the next shock cell, the jet is reattached to the Coanda surface with the help of a favorable pressure gradient. After separation, the jet is reattached to the Coanda surface to generate a separation bubble structure. At $NPR = 4$, the shock cell structure is smaller. When the jet is attached, the shock cell structure basically disappears without an obvious separation bubble. At $NPR = 6$ and $NPR = 7$, the size of the shock cell structure increases. When the jet is attached, the shock cell structure still exists, so a separation bubble is generated. At $NPR = 8$, there is no periodic shock structure, so no separation bubble is generated.

At $NPR = 4$, the jet starts to attach at $\theta = 34^\circ$ and separates at $\theta = 87^\circ$. At $NPR = 6$, the jet starts to attach at $\theta = 38^\circ$ and separates at $\theta = 86^\circ$. The jet attachment area is basically unchanged, but the jet momentum increases. The mixing effect between the jet and the low-speed area of the main wing wake is enhanced, and more energy is transferred to the wake, so the lift increases. At $NPR = 7$, the jet reattaches at $\theta = 41^\circ$ and separates at $\theta = 70^\circ$. The jet momentum increases. The jet separates prematurely on the Coanda surface as a result of the insufficient centripetal force provided by the pressure difference. At $NPR = 8$, under the action of the inner shear layer, the momentum on the near wall decreases and the adhesion capability of the jet is enhanced. The jet separates at $\theta = 75^\circ$. Compared with

$NPR = 7$, the separation point at the trailing edge moves backward, so the lift coefficient is slightly increased.

Figure 17 shows the Mach number cloud diagram at the trailing edge under different jet pressure ratios. As we can see, at $NPR = 6$, the jet is the best at accelerating the upper flow. Figure 18 shows the comparison of the tangential velocity profiles at different θ . The jet is of the converging nozzle and step structure. At $\theta = 0^\circ$, the velocity at the jet exit is basically the same under different jet pressure ratios. At $\theta = 60^\circ$, the near-wall velocity profiles at $NPR = 6$ and $NPR = 7$ are basically consistent. However, from the comparison of the pressure coefficients, at $NPR = 6$, the negative pressure on the Coanda surface is greater at $\theta = 60^\circ$, and the greater pressure difference promotes jet attachment. At $\theta = 90^\circ$, significant flow separation occurred at $NPR = 7$ and $NPR = 8$, and there is still a high tangential velocity at $NPR = 6$. At $NPR = 8$, because of the effect of normal shock, the velocity in the middle of the jet is small, while the velocity on both sides of the jet is fast, and the tangential velocity profile is “M” shaped. Under the combined action of the inner and outer shear layers, the jet momentum decays rapidly.

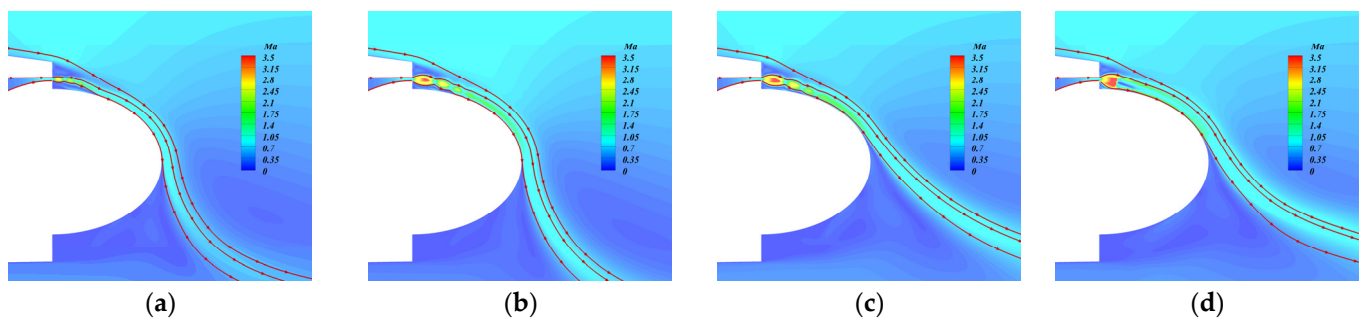


Figure 17. Mach number cloud diagram at the trailing edge: (a) $NPR = 4$, (b) $NPR = 6$, (c) $NPR = 7$, and (d) $NPR = 8$.

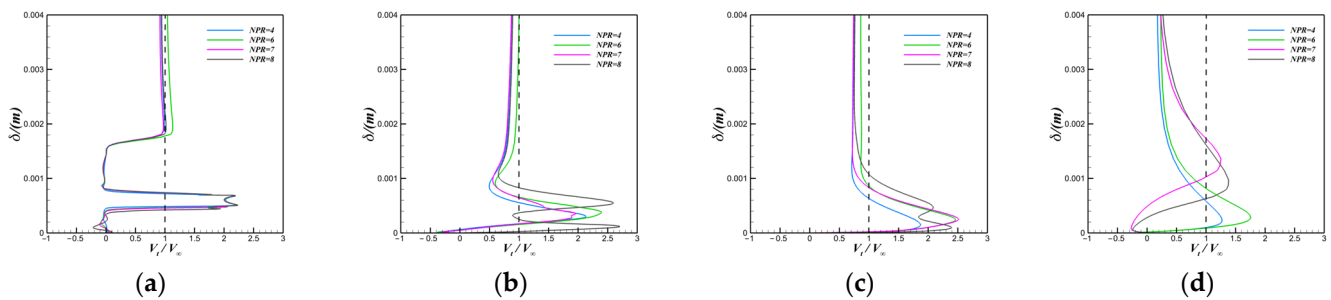


Figure 18. Comparison of tangential velocity at different θ location: (a) $\theta = 0^\circ$; (b) $\theta = 30^\circ$; (c) $\theta = 60^\circ$; (d) $\theta = 90^\circ$.

4.2. Impact Analysis of Ellipticity

A configuration with a nozzle height $h = 0.2$ mm and back-facing step height $t = 0.5$ mm is selected to study the impact of different ellipticity on the aerodynamic characteristics and flow field structure of CC airfoil when the jet pressure ratio is $NPR = 6$.

Figure 19 shows the variation trend of the lift coefficient with the ellipticity. As the ellipticity increases, the lift coefficient increases and then decreases. Figure 20 shows the pressure coefficients on the airfoil surface. At $a/b = 1.5$ and $a/b = 2.0$, the pressure surface and suction surface pressure coefficients of the airfoil change significantly. The pressure distribution pattern is similar, and the absolute value of the pressure increases relative to the initial configuration. At $a/b = 1.5$, the absolute value of the pressure coefficient increases the most, and “virtual rudder surface” works the best.

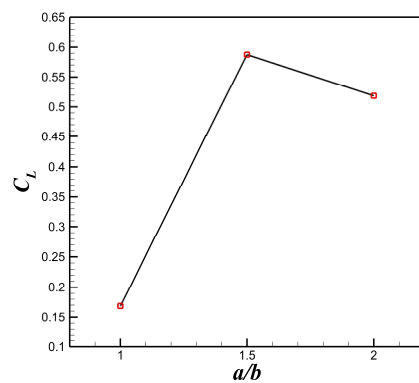


Figure 19. Variation trend of the lift coefficient with the ellipticity.

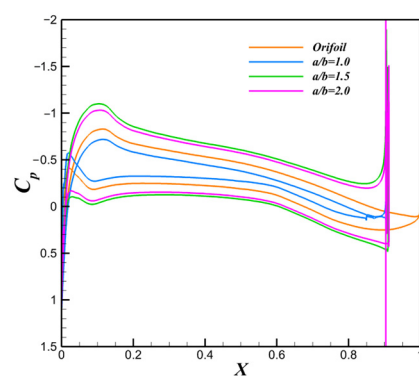


Figure 20. Airfoil surface pressure coefficient.

Figure 21 shows the Mach number cloud diagram at the trailing edge of the CC airfoil. At $a/b = 1.0$, the Coanda profile is a circular trailing edge with a constant curvature. The centripetal force provided by the pressure difference is insufficient for the jet to remain attached to the wall. The flow structure near the nozzle exit is similar to that of the free jet, and the Coanda surface is completely separated, so it is unable to produce the lift augmentation effect. With the increase in ellipticity, the profile near the nozzle exit is closer to the plane, and the angle of jet deflection per unit flow length decreases, and the centripetal force required for jet deflection is reduced, which contributes to jet attachment. At $a/b = 1.5$, the jet is attached to the Coanda surface well. As the ellipticity increases again, the initial curvature of the Coanda surface is small at $a/b = 2.0$, and the jet is easily attached. However, along the direction of the jet flow, the curvature gradually increases and the centripetal force required for the jet attachment increases, which is not conducive to flow attachment, so the jet is separated in advance.

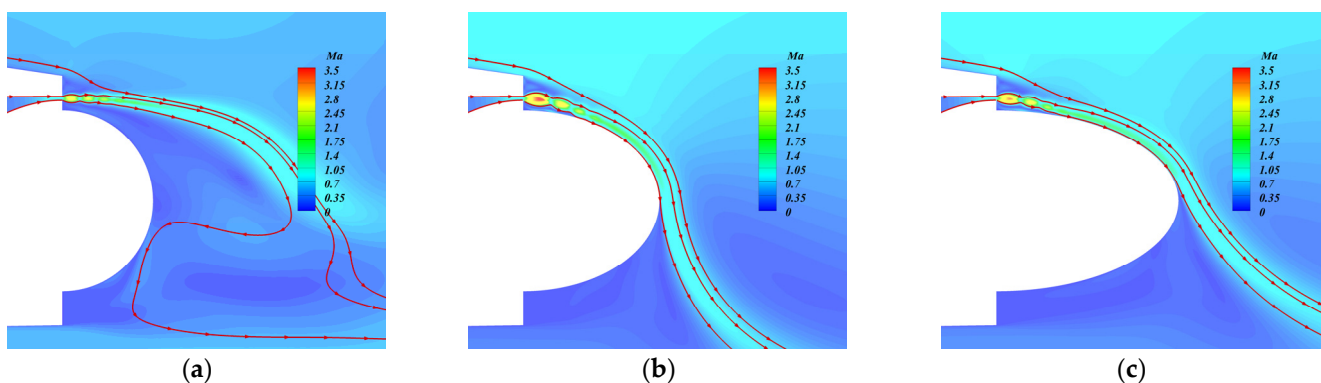


Figure 21. Mach number cloud diagram at the trailing edge: (a) $a/b = 1.0$, (b) $a/b = 1.5$, and (c) $a/b = 2.0$.

Figure 22 shows the Schlieren images of configurations with different ellipticities. We can see that ellipticity has an impact on the size of the shock cell. The flow characteristics downstream of the jet will feed back to the upstream to change the strength of shock cells at the jet exit. If the jet is well attached to the Coanda surface, it will promote the expansion of the jet at the nozzle and increase the size of the shock cell.

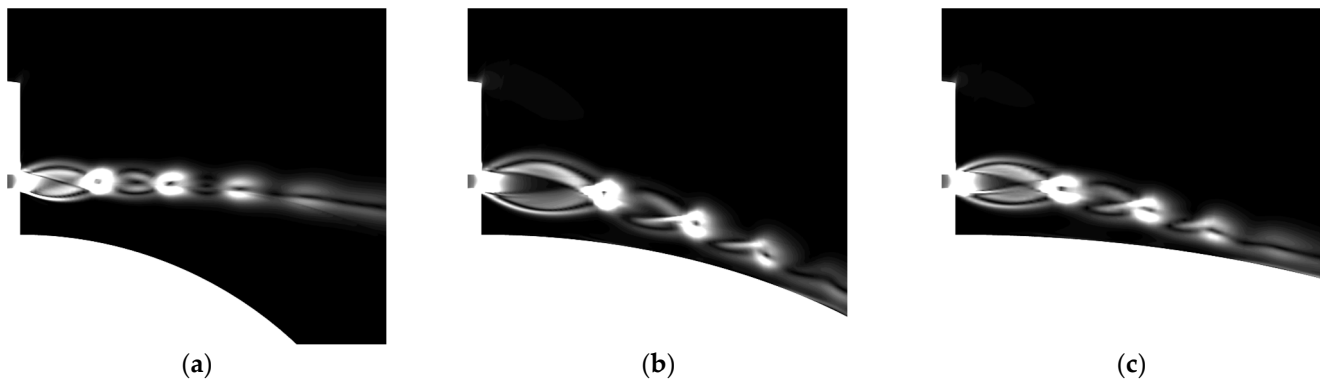


Figure 22. Schlieren image: (a) $a/b = 1.0$, (b) $a/b = 1.5$, and (c) $a/b = 2.0$.

Figure 23 shows the comparison of the pressure coefficient and tangential velocity on the Coanda surface. At $a/b = 1.5$ and $a/b = 2.0$, there is a favorable pressure gradient at about $\theta = 35^\circ$, and the jet begins to attach to the Coanda surface. At $a/b = 1.5$, the curvature of the Coanda surface changes little, and the pressure distribution changes slightly after jet attachment. The jet begins to attach at $\theta = 38^\circ$ and separates at $\theta = 86^\circ$. At $a/b = 2.0$, the curvature of the Coanda surface changes greatly. The jet velocity on the Coanda surface is fast after jet attachment, and the negative pressure on the surface tends to increase. The jet begins to attach at $\theta = 34^\circ$ and separates at $\theta = 82^\circ$. The separation position moves forward. Therefore, the ellipticity should be moderate. In the case of small ellipticity, the jet cannot attach to the Coanda surface. In the case of large ellipticity, the effective deflection angle of the jet decreases and the jet control efficiency is reduced.

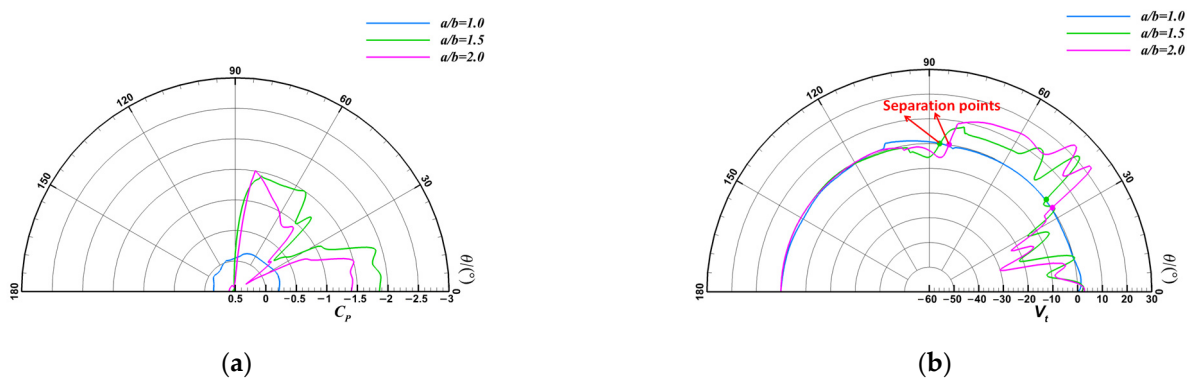


Figure 23. Comparison of the pressure coefficient and tangential velocity on the Coanda surface: (a) comparison of the pressure coefficient on the Coanda surface and (b) comparison of the tangential velocity on the Coanda surface.

4.3. Impact Analysis of Nozzle Height

A configuration with ellipticity $a/b = 1.5$ and back-facing step height $t = 0.5$ mm is selected to study the impact of different nozzle heights on the aerodynamic characteristics and flow field structure of the CC airfoil when the jet pressure ratio is $NPR = 8$.

Figure 24 shows the variation trend in the lift coefficient with the nozzle height. As the nozzle height increases, the lift coefficient tends to decrease. Figure 25 shows the Mach number cloud diagram at the trailing edge of the airfoil. As the nozzle height increases, the jet momentum increases and the size of shock cell increases significantly. Moreover,

the centripetal force provided by the pressure difference is insufficient, the adhesion capability of the jet is reduced, and the separation position moves forward. Figure 26 shows a comparison of the pressure coefficient and tangential velocity on the Coanda surface. At $h = 0.1$ mm, the jet separates at $\theta = 95^\circ$. At $h = 0.2$ mm, the jet separates at $\theta = 75^\circ$. At $h = 0.3$ mm, the jet separates at $\theta = 56^\circ$, and the jet separation position decreases equidistantly by about 20° .

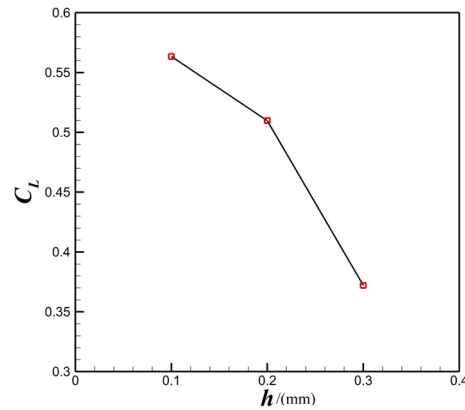


Figure 24. Variation trend of the lift coefficient with the nozzle height.

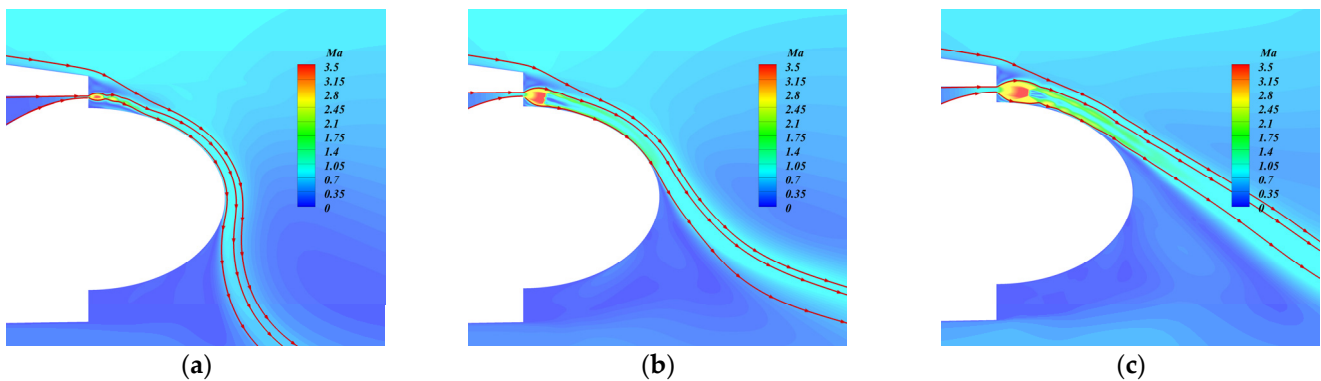


Figure 25. Mach number cloud diagram at the trailing edge: (a) $h = 0.1$ mm, (b) $h = 0.2$ mm, and (c) $h = 0.3$ mm.

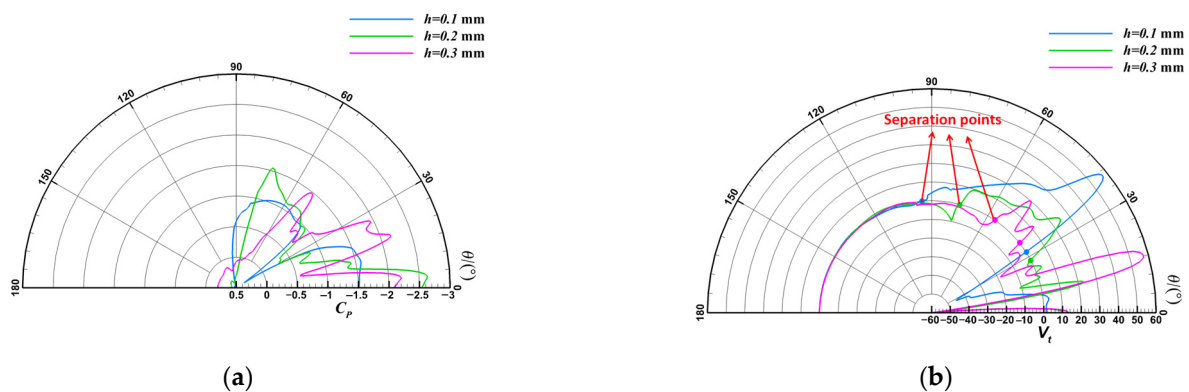


Figure 26. Comparison of the pressure coefficient and tangential velocity on the Coanda surface: (a) comparison of the pressure coefficient on the Coanda surface and (b) comparison of the tangential velocity on the Coanda surface.

Figure 27 shows the Mach number cloud diagram at the jet exit, and Figure 28 shows the Schlieren image at the exit. At $h = 0.1$ mm, the size of the shock cell is smaller. At $\theta = 32^\circ$,

under the effect of a favorable pressure gradient, the jet is attached to the wall, no shock cell is generated after the attachment, and the attachment state is good. At $h = 0.2$ mm, the intercepting shock formed by the reflection of the jet after expansion is strong. The intercepting shocks on both sides meet and generate Mach reflection, forming a strong normal shock. The jet behind the normal shock is subsonic. The reflecting shocks on both sides of the jet are small in size. The jet remains in supersonic flow after passing through the reflecting shock (oblique shock). The jet is bifurcated, and the energy of the bifurcated jet near the wall is small. There is no sub-shock cell structure, and the jet still remains attached. At $h = 0.3$ mm, the strength of the lower intercepting shocks increases under the action of wall extrusion. The Mach disk formed after the intercepting shocks on both sides meet is small in size, while the reflecting shocks on both sides are larger. After passing through the intercepting shock, the jet loses less momentum. After the jet is bifurcated, the bifurcated jet near the wall forms a sub-shock cell structure. Therefore, at $h = 0.3$ mm, the vibration frequency of the pressure distribution on the Coanda surface increases, and the adhesion capability of the jet is significantly reduced.

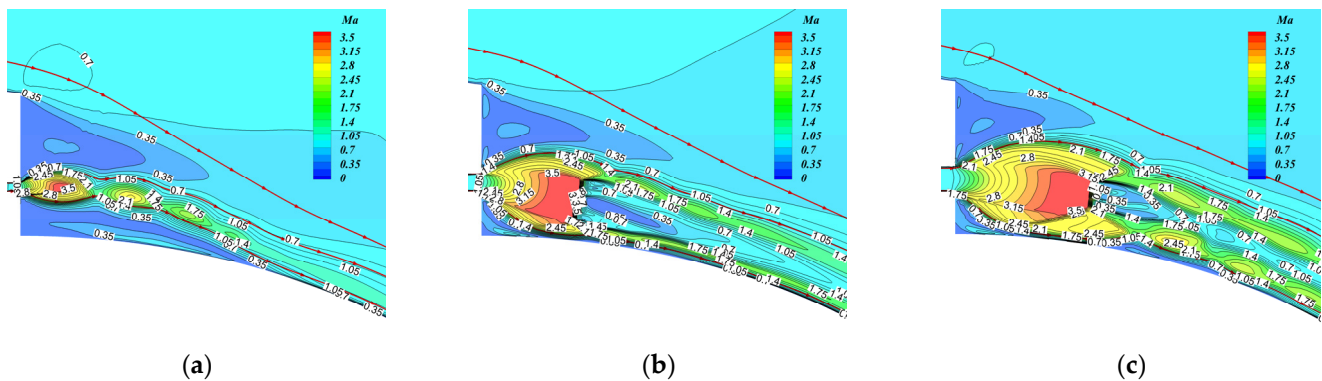


Figure 27. Mach number cloud diagram at the jet exit: (a) $h = 0.1$ mm, (b) $h = 0.2$ mm, and (c) $h = 0.3$ mm.

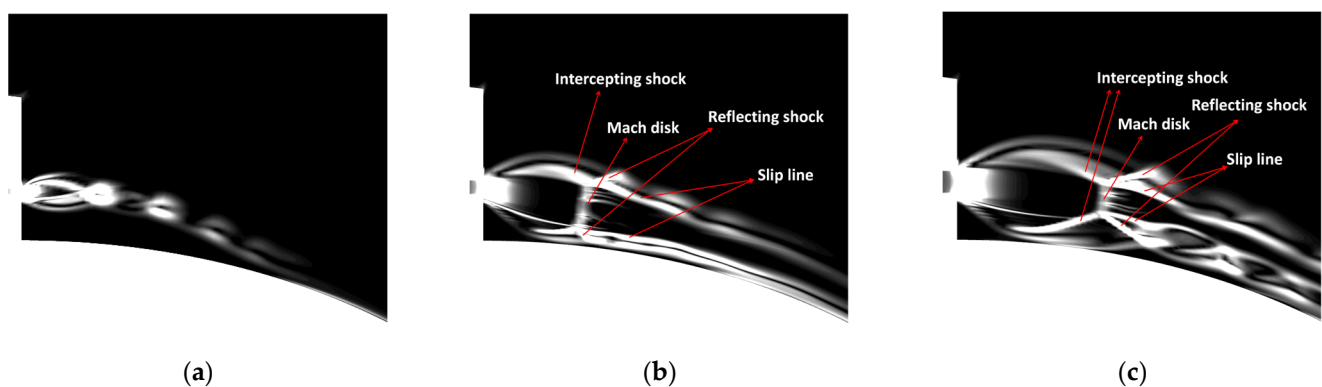


Figure 28. Schlieren image: (a) $h = 0.1$ mm, (b) $h = 0.2$ mm, and (c) $h = 0.3$ mm.

5. Conclusions

Through numerical simulation of the CC airfoil with a converging nozzle and step structure at the trailing edge, we studied the effect of the jet pressure ratio and geometric design parameters of the trailing edge on the flow field structure of the under-expansion jet and aerodynamic characteristics of CC airfoil, and reached the following conclusions:

1. A converging nozzle and step structure provides expansion space for the under-expansion jet of CC airfoil and changes the shock–boundary layer interaction form. The combination design of proper ellipticity and the back-facing step contributes to forming a closed low-pressure vortex area behind the step, promoting jet attachment and improving the jet attachment pressure ratio effectively.

2. As the jet pressure ratio increases, the entrainment effect of the jet on the upper airfoil and the blocking effect of the jet on the lower airfoil are enhanced, and the lift coefficient increases. When the critical stall pressure ratio is exceeded, the size of the shock cell at the exit is larger, the adhesion capability of the jet is reduced, and the lift coefficient decreases. When the jet pressure ratio increases again, the intercepting shocks on both sides meet and generate Mach reflection. After jet stratification, the adhesion capability of the jet is improved and the lift coefficient is slightly increased.
3. As the ellipticity increases, the lift coefficient increases and then decreases. With the optimal ellipticity, the “virtual rudder surface” of the jet works best. The curvature at the exit and the curvature at the jet separation should be taken into account in the selection of ellipticity. In order to improve the jet control efficiency, the curvature change rate of the Coanda profile should be reduced as much as possible after the jet is attached at the exit.
4. At a high jet pressure ratio, as the nozzle height increases, the jet momentum and thickness increase, and the adhesion capability of the jet is reduced. At $h = 0.3$ mm, the shock structure at the jet exit stratifies the jet, and the bifurcated jet near the wall forms a sub-shock cell structure, which is not conducive to jet attachment. Reducing the nozzle height can improve the adhesion capability of the jet at a high pressure ratio.
5. The next research direction is to study the stability of under-expanded jet based on the high precision numerical simulation methods (such as DDES and LES). A wind tunnel experimental study on jet circulation control airfoil is also carried out to study the structural details of the supersonic Coanda jet field using some test equipment and flow field measurement means.

Author Contributions: Conceptualization, M.H. and L.Z. (Liu Zhang); methodology, M.H.; validation, M.H.; formal analysis, M.H. and L.Z. (Liu Zhang); investigation, M.H., C.L. and L.Z. (Lei Zhao); resources, L.Z. (Liu Zhang); data curation, M.H. and C.L.; writing—original draft preparation, M.H.; writing—review and editing, M.H. and L.Z. (Liu Zhang); visualization, M.H.; supervision, L.Z. (Liu Zhang); project administration, L.Z. (Liu Zhang). All authors have read and agreed to the published version of the manuscript.

Funding: This research received no external funding.

Data Availability Statement: The data that support the findings of this study are available from the corresponding author upon reasonable request.

Conflicts of Interest: The authors declare no conflict of interest. The funders had no role in the design of the study; in the collection, analyses, or interpretation of data; in the writing of the manuscript; or in the decision to publish the results.

Abbreviations

RANS	Reynolds averaged Navier–Stokes equation
CC	Circulation control
CFD	Computational fluid dynamics
NASA	National aeronautics and space administration
TDT	Langley transonic dynamics tunnel
LES	Large eddy simulation
STOL	Short takeoff and landing
ICE	Innovative control effectors
EXP	Experiment
UAV	Unmanned aerial vehicle

References

1. Metral, A.R. On the Phenomenon of Fluid Veins and Their Application, the Coanda Effect. *AF Transl. F-TS-786-RE* **1939**.
2. Englar, R.J. *Two-Dimensional Transonic Wind Tunnel Tests of Three 15-Percent Thick Circulation Control Airfoils*; David W. Taylor Naval Ship Research and Development Center: Washington, DC, USA, 1970.
3. Englar, R.J. *Two-Dimensional Subsonic Wind Tunnel Tests of Two 15-Percent Thick Circulation Control Airfoils*; David W. Taylor Naval Ship Research and Development Center: Washington, DC, USA, 1971.
4. Englar, R.J. *Low-Speed Aerodynamic Characteristics of a Small, Fixed-Trailing-Edge Circulation Control Wing Configuration Fitted to a Supercritical Airfoil*; David W. Taylor Naval Ship Research and Development Center, Bethesda Md Aviation and Surface Effects Dept: Washington, DC, USA, 1981.
5. Abramson, J. *Two-dimensional Subsonic Wind Tunnel Evaluation of Two Related Cambered 15-Percent Thick Circulation Control Airfoils*; David W. Taylor Naval Ship Research and Development Center, Bethesda Md Aviation and Surface Effects Dept: Washington, DC, USA, 1977.
6. Novak, C.; Cornelius, K.; Roads, R. Experimental Investigations of the Circular Wall Jet on a Circulation Control Airfoil. In Proceedings of the 25th AIAA Aerospace Sciences Meeting, Reno, NV, USA, 24–26 March 1987. [[CrossRef](#)]
7. NTRS—NASA Technical Reports Server. Available online: <https://ntrs.nasa.gov/api/citations/20050165090/downloads/20050165090.pdf> (accessed on 11 November 2021).
8. Swanson, R.C.; Rumsey, C.L. Computation of Circulation Control Airfoil Flows. *Comput. Fluids* **2009**, *38*, 1925–1942. [[CrossRef](#)]
9. Nishino, T.; Hahn, S.; Shariff, K. Large-Eddy Simulations of a Turbulent Coanda Jet on a Circulation Control Airfoil. *Phys. Fluids* **2010**, *22*, 125105. [[CrossRef](#)]
10. Rumsey, C.L.; Nishino, T. Numerical Study Comparing RANS and LES Approaches on a Circulation Control Airfoil. *Int. J. Heat Fluid Flow* **2011**, *32*, 847–864. [[CrossRef](#)]
11. Williams, D.R.; Seidel, J.; Osteros, R. NATO AVT-239 Task Group: Flight Control Derivatives using Active Flow Control Effectors on the ICE/SACCON USA Model. In Proceedings of the AIAA Scitech 2019 Forum, San Diego, CA, USA, 7–11 January 2019. [[CrossRef](#)]
12. Smith, D.; Warsop, C. NATO AVT-239 Task Group: ‘Innovative Control Effectors for Manoeuvring of Air Vehicles’—Introduction and overview. In Proceedings of the AIAA Scitech 2019 Forum, San Diego, CA, USA, 7–11 January 2019. [[CrossRef](#)]
13. Savvaris, A.; Buonanno, A.; Jamil, R.; Tsourdos, A. Design and Development of the DEMON UAV Fluidic Flight Control System. In Proceedings of the AIAA Infotech @ Aerospace (I @ A) Conference, Boston, MA, USA, 19–22 August 2013. [[CrossRef](#)]
14. Warsop, C.; Crowther, W. NATO AVT-239 Task Group: Flight Demonstration of Fluidic Flight Controls on the MAGMA Subscale Demonstrator Aircraft. In Proceedings of the AIAA Scitech 2019 Forum, San Diego, CA, USA, 7–11 January 2019. [[CrossRef](#)]
15. Zhang, L.; Huang, Y.; Zhu, Z.L. Virtual Flight Test of Pitch and Roll Attitude Control Based on Circulation Control of Tailless Flying Wing Aircraft Without Rudders. *Chin. J. Aeronaut.* **2023**. [[CrossRef](#)]
16. Gregory-Smith, D.G.; Senior, P. The Effects of Base Steps and Axisymmetry on Supersonic Jets over Coanda Surfaces. *Int. J. Heat Fluid Flow* **1994**, *15*, 291–298. [[CrossRef](#)]
17. Carpenter, P.W.; Green, P.N. The Aeroacoustics and Aerodynamics of High-Speed Coanda Devices, PART 1: Conventional Arrangement of Exit Nozzle and Surface. *J. Sound Vib.* **1997**, *208*, 777–801. [[CrossRef](#)]
18. Forster, M.; Steijl, R. Numerical simulation of transonic circulation control. In Proceedings of the 53rd AIAA Aerospace Sciences Meeting, Kissimmee, FL, USA, 5–9 January 2015. [[CrossRef](#)]
19. Llopis-Pascual, A. Supercritical Coanda Jets for Flight Control Effectors. Ph.D. Thesis, Manchester University, Manchester, UK, 2016.
20. Wang, Q.; Qu, F.; Zhao, Q.; Bai, J. Numerical Study of the Hysteresis Effect on the Supercritical Airfoil for the Transonic Circulation Control. *Aerosp. Sci. Technol.* **2022**, *126*, 107645. [[CrossRef](#)]

Disclaimer/Publisher’s Note: The statements, opinions and data contained in all publications are solely those of the individual author(s) and contributor(s) and not of MDPI and/or the editor(s). MDPI and/or the editor(s) disclaim responsibility for any injury to people or property resulting from any ideas, methods, instructions or products referred to in the content.